



Unravelling the Tip Effect of Oxygen Catalysis in Integrated Cathode for High-Performance Flexible/Wearable Zn–Air Batteries

Yirun Shen¹ · Haoning Mao¹ · Chen Li¹ · Keer Li¹ · Yi Liu¹ · Jihai Liao² · Shengsen Zhang² · Yueping Fang¹ · Xin Cai¹

Received: 5 January 2024 / Accepted: 23 April 2024 / Published online: 15 May 2024
© Donghua University, Shanghai, China 2024

Abstract

The exploration of high-efficiency transition metal–nitrogen–carbon (M–N–C) catalysts is crucial for accelerating the kinetics of oxygen reduction/oxygen evolution reactions (ORR/OER). Fine-tuning the distribution of accessible metal sites and the correlated triphase interfaces within the M–N–C catalysts holds significant promise. In this study, we present an integrated electrocatalyst comprised of tip-enriched NiFe nanoalloys encapsulated within N-doped carbon nanotubes (NiFe@CNTs), synthesized using an *in-situ* wet-electrochemistry mediated approach. The well-defined NiFe@CNTs catalyst possesses a porous heterostructure, synergistic M–N_x–C active sites, and intimate micro interfaces, facilitating accelerated redox kinetics. This leads to exceptional OER/ORR activities with a low overall ΔE of 630 mV. Experimental results and density functional theory calculations unveil the predominant electronic interplay between the apical bimetallic sites and neighboring N-doped CNTs, thereby enhancing the binding of intermediates on NiFe@CNTs. Molecular dynamics simulations reveal that the local gas–liquid environment surrounding NiFe@CNTs favors the diffusion/adsorption of the OH[−]/O₂ reactants. Consequently, NiFe@CNTs contribute to high-performance aqueous Zn–Air batteries (ZABs), exhibiting a high gravimetric energy density (936 Wh kg_{Zn}^{−1}) and superb cycling stability (> 425 h) at 20 mA cm^{−2}. Furthermore, solid-state ZABs based on NiFe@CNTs demonstrate impressive electrochemical performance (e.g., peak power density of 108 mW cm^{−2}, specific energy of 1003 Wh kg_{Zn}^{−1}) and prominent flexibility. This work illuminates a viable strategy for constructing metal site-specific, cobalt-free, and integrated M–N–C electrocatalysts for multifunctional catalysis and advanced/flexible energy storage applications.

Keywords Flexible Zn–air batteries · Bimetal alloys · M–N–C catalysts · Tip effect · Triphase reaction interfaces

1 Introduction

The imperative shift towards a low-carbon economy and the escalating global energy consumption necessitates the development of high-performance renewable energy storage systems. Among these, the rechargeable zinc–air battery (ZAB) becomes a promising option due to its high specific energy (1218 Wh kg^{−1}), low cost, reliable security features, and long-term rechargeability [1, 2]. However, the

constrained kinetics of oxygen reduction/oxygen evolution reactions (ORR/OER), characterized by intricate multi-proton/electron transfer pathways, pose a significant bottleneck. Addressing this challenge requires suitable bifunctional catalysts at the air cathode to reduce charge/discharge polarization and promote the electrochemical performance of existing ZABs [3–5]. Platinum-group precious metals (Pt, Ir, and Ru) have historically dominated the catalysis of oxygen electrochemistry, yet their scarcity and limited catalytic tolerance have impeded large-scale application [6]. Therefore, the pursuit of intrinsically active, stable, and inexpensive bifunctional catalysts is vital for advancing rechargeable ZABs [7]. In addition, traditional slurry-casting methods for cathodes typically involve the loading of electrocatalysts onto conductive substrates using adhesives/binders [8]. However, these inert binders and suboptimal interfacial contacts between the electrocatalysts and the conductive substrates diminish the accessibility of active sites on the catalyst surfaces, ultimately compromising battery

✉ Xin Cai
caixin2015@scau.edu.cn

¹ Key Laboratory for Biobased Materials and Energy of Ministry of Education, Guangdong Laboratory for Lingnan Modern Agriculture, College of Materials and Energy, South China Agricultural University, Guangzhou 510642, China

² Department of Physics, South China University of Technology, Guangzhou 510640, China

performance during prolonged cycling or under intensified mechanical stress [9]. To address this issue, a prevailing strategy involves the rational construction of binder-free, self-supporting electrocatalysts through the direct bottom-up growth of active species on the conductive supports without the use of binders [10]. Nevertheless, achieving ideal binder-free electrocatalysts with superior bifunctionality, high durability, and mechanical resilience for oxygen catalysis and practical ZABs remains a formidable challenge [11].

Among various non-precious metal-based electrocatalysts, transition metals with elaborate nanoarchitecture or atomically dispersed within a nitrogen-doped carbon matrix, i.e., heterogeneous M@NC (M = Fe, Co, Ni, etc.) oxygen electrocatalysts, emerge as state-of-the-art candidates [12–14]. Considerable efforts focus on engineering the single-metal reactive sites through extrinsic (e.g., morphological features, hierarchical porosity, surface/interfacial contact area, etc.) or intrinsic (e.g., phase composition, local atomic structure, and chemical coordination environment, etc.) regulations to enhance the electron transfer and mass transport of the bifunctional catalysts for improved OER/ORR activities [15–20]. Introducing a second metal into M@NC facilitates further modulation of the electronic/geometric structure of single metal sites due to synergistic bimetallic interplay and adjustable M–N_x configuration. This enhances the bonding strength between the active centers and the oxo-intermediates leading to increased utilization efficiency of the catalytic atoms [21–24]. Therefore, the distribution and stabilization of highly unsaturated metal centers become indispensable within a heteroatom-doped carbonaceous matrix via metal-support interactions [25, 26]. Nonetheless, most M@NC catalysts, formed through the copyrolysis of metal, carbon, and nitrogen precursors, such as the metal–organic–framework (MOF) precursors, may suffer from insufficient tuning of the morphology homogeneity and the local structure surrounding the reactive sites, particularly when bimetallics are concurrently incorporated [23, 27, 28]. To achieve balanced adsorption of intermediates over competitive OER/ORR sites along respective reaction paths, it is profoundly significant to increase the active-site density (metal loading of > 3 wt%) and precisely regulate the local chemical environment of the bimetal active sites in the bifunctional catalysts [29].

Preferably, arrays of N-doped carbon nanotubes (NCNTs) have exhibited impressive attributes for constructing efficient M@NCNTs catalysts, benefiting from directional channels that facilitate electron and ion transport [30]. However, the hydrophobic nature of typical NCNTs and the random distribution of metal nanoparticles (NPs) on their surfaces may interfere with the entry of H₂O/OH[−], oxygen molecules, and other intermediates into the interior metal active sites within the CNTs [31]. To achieve highly active M@NCNTs catalysts, simple and universal synthesis of dual

metal sites at the target locations in dense, defect-rich CNTs holds immense promise, though it is rarely reported [32]. In addition to tailoring active species on the catalyst surface, establishing stable and optimal gas (O₂)–solid (catalyst)–liquid (electrolyte) interfaces of the electrocatalysts is equally important [33]. The complete OER/ORR process occurring at the triphase zone is complex, involving interrelated key steps of O₂/electrolyte diffusion, multi-step electron transfer, and surface reactions on the active sites [34]. Enhancing the utilization efficiency of active sites and bifunctional oxygen catalysis can be achieved by forming desirable triphase reaction interfaces with moderate hydrophobicity/hydrophilicity and effective contact area. Feng et al. recently discovered that a porous carbon host with curved surfaces can effectively engineer the local coordination microenvironment of FeN₄ sites by modifying the Fe *d*-band centers, contributing to superior ORR performance [35]. Accordingly, if metal active sites are intentionally grown at the apex of highly-curved NCNTs, the synergistic interactions of bimetal–N–C moieties may energetically activate the reaction sites and further optimize the correlated three-phase interfaces simultaneously [12]. Moreover, by mimicking the apical growth mechanism of natural plants, such top-dominant active sites have better access to O₂/OH[−] reactants for desirable oxygen catalysis compared to lateral or bottom active sites in conventional M@NCNTs-based catalysts.

In response to the aforementioned concerns, we have developed self-supporting and integrated electrocatalysts comprising tip-enriched NiFe nanoalloys encapsulated within NCNT arrays (denoted as NiFe@CNTs). The well-designed NiFe@CNTs were synthesized in situ using a convenient wet-electrochemistry-mediated approach. Specifically, pre-rooted bimetallic NiFe nanoalloys served as patterned templates and catalytic seeds for the apical growth of NCNT nanoarrays, concomitantly wrapping the metal NPs during the vapor deposition process. Leveraging the advantages of a 3D interconnected conductive network, porous heterostructure for mass transfer, and especially tip-enriched bimetallic sites, NiFe@CNTs exhibited exceptional bifunctional activities with a low overpotential of 220 mV at 10 mA cm^{−2} and a half-wave potential (*E*_{1/2}) of 0.82 V. Both experimental and theoretical results unveiled the tip-effect of the nanoalloys, strongly interacting with active NCNTs to promote the electronic synergism of M–N_x–C, favoring appropriate reactant/intermediate adsorption and balanced hydrophilicity for improved three-phase reaction interfaces. The superiority of the NiFe@CNTs electrocatalyst was further illuminated as a binder-free air cathode in both aqueous ZABs and solid-stated flexible ZABs, yielding high specific capacities, impressive peak power density, outstanding rate capabilities, and prominent cycling stability. This work elucidates the enhanced utilization efficiency of metal site-specific and integrated M–N–C electrocatalysts,

providing an alternative strategy for designing multifunctional heterogeneous catalysts for advanced/flexible energy storage applications.

2 Results and Discussion

2.1 Morphology and Composition of Catalysts

The self-supported NiFe@CNTs catalyst was synthesized via an in-situ route which combines facile electrodeposition/etching with a catalytic vapor deposition process. As illustrated in Fig. 1a, NiFeCu consisting of dense NP aggregates were initially deposited onto carbon cloth (CC) fibers by applying a voltage of -0.75 V at room temperature (Fig. S1, Fig. S2a, b). Subsequently, applying a reverse voltage of $+0.3$ V selectively etched/oxidized metallic Cu to Cu^{2+} , which dissolved to generate NiFe, as confirmed by the prominent diffraction peaks

corresponding to the (1 1 1), (2 0 0), and (2 2 0) planes of NiFe alloys (JCPDs No. 47–1417, Fig. S3). Scanning electron microscope (SEM) images of NiFe in Fig. 1b reveal its ordered porous structure of hollow nanoflowers after electroetching. Ultimately, the uniformly rooted NiFe nanoalloys act as a patterned template and available seeds to actively catalyze the upward growth of CNTs through typical vapor–liquid–solid (V–L–S) deposition, using dicyandiamide (DCD) as the carbon/nitrogen source [36]. As shown in Fig. 1c, the obtained NiFe@CNTs possess neat and vertically aligned nanoarrays with top-concentrated bright metal NPs (as indicated by the red dashed circles). X-ray diffraction (XRD) patterns of NiFe@CNTs exhibit a strong graphitic-carbon peak located near 26° , along with weakened peaks of NiFe alloy as compared to NiFe (Fig. S3), implying the encapsulation of NiFe nanoalloys by carbon layers. The loading of nickel and iron in CC-supported NiFe@CNTs is determined to be 3.83 wt% and 0.73 wt% according to inductively coupled

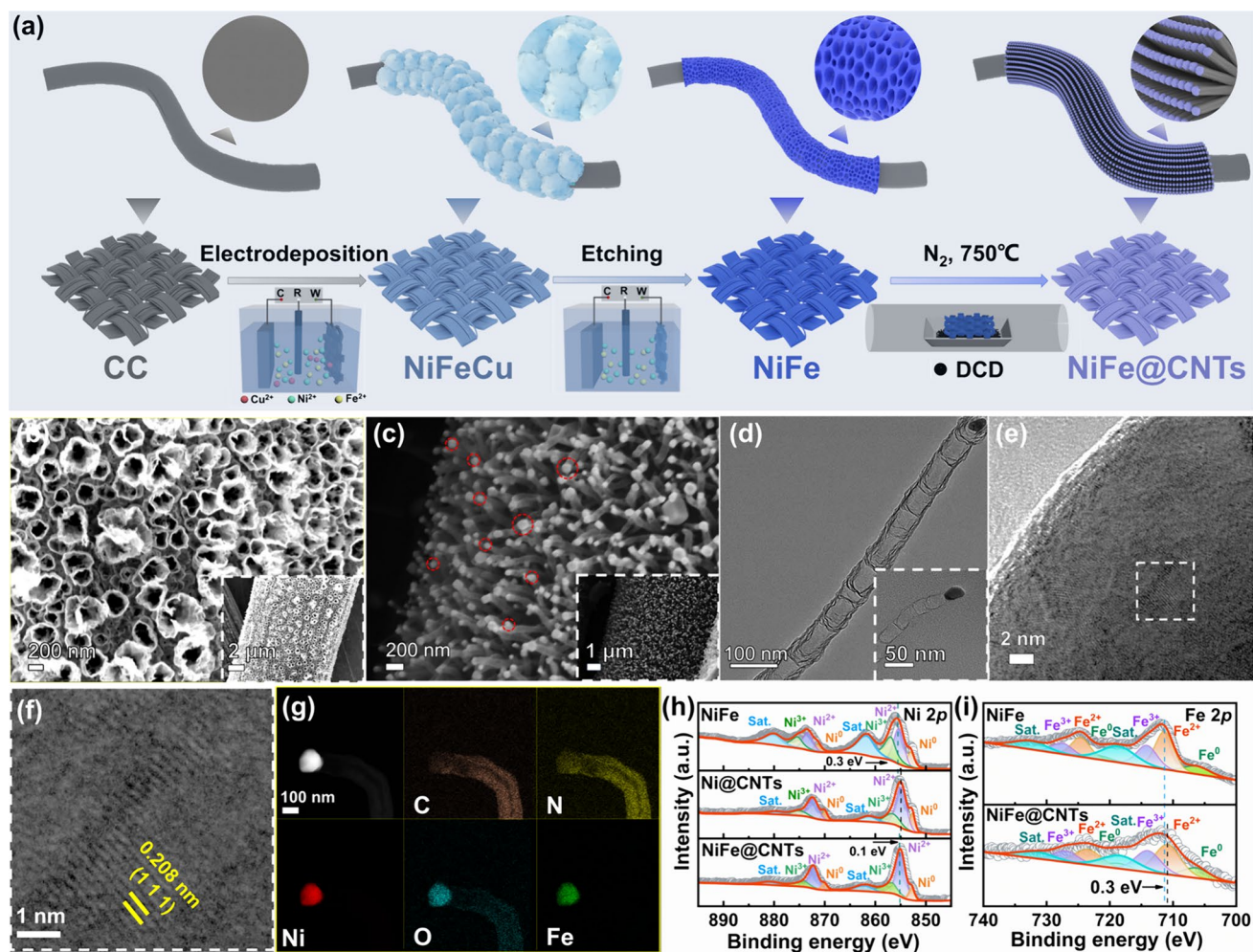


Fig. 1 a Scheme for the synthesis of self-supported NiFe@CNTs. SEM image of **b** NiFe. **c** NiFe@CNTs. **d–f** HR-TEM images of NiFe@CNTs. **g** EDS elemental mapping images of NiFe@CNTs. High-resolution XPS spectra for NiFe, Ni@CNTs and NiFe@CNTs. **h** Ni 2p. **i** Fe 2p

plasma optical emission spectrometer (ICP-OES) tests (Table S1). Through such a wet-electrochemistry-regulated synthetic approach, the produced monolithic NiFe@CNTs catalysts are significantly robust with excellent mechanical bendability and superior electrical conductivity due to seamlessly bonded nanoarrays catalysts with a 3D porous CC substrate (Fig. S4a-d).

High-resolution transmission electron microscopy (HR-TEM) images of NiFe@CNTs reveal the bamboo-shaped CNTs with a radial size of 50–100 nm, wherein the top domain of curved carbon layers tightly encases spherical NPs (Fig. 1d, e). The lattice spacings of 0.127 nm, 0.180 nm, and 0.208 nm of the internal NPs correspond to the (2 2 0), (2 0 0), and (1 1 1) crystalline planes of the alloyed NiFe phase in NiFe@CNTs (Fig. 1f) [37]. Figure 1g shows the energy disperse spectroscopy (EDS) elemental maps of NiFe@CNTs, where C and N elements are uniformly spread in the entire CNT matrix, while Ni, Fe, and O elements are interspersed within the top region of N-doped CNT. Relevant quantitative analysis demonstrates that the mass fraction ratio of Ni: Fe is 3.67:1, approximating the aforementioned ICP result (Fig. S5a, b, Table S2). These results further validate the construction of structurally ordered N-doped CNTs with tip-enriched and encapsulated NiFe nanoalloys. This unique structure of NiFe@CNTs is primarily attributed to the electrodeposited NiFe nanoalloys with small particle size, patterned nanopores, and suitable bimetal composition, essential for catalyzing the closed-end tip growth of N-doped CNTs by spontaneously incorporating the metallic NPs within the tip through excessive segregation/precipitation of carbon vapor and dynamic reconstruction of the nanotube tip [38]. For comparison, both NiFe-N@CNTs (Fig. S6a, Fig. S7, synthesized with directly electrodeposited NiFe alloys on CC without electroetching to form a porous structure) and Ni@CNTs (synthesized without Fe inclusion) (Fig. S8a, b) demonstrate random orientation of CNTs and multiple distribution of partial metal NPs inside the nanotubes rather than completely tip-enriched. By varying the precursor salt bath, electrodeposition voltage, and etching potentials, other self-supported catalysts of monometal (Ni) or bimetallic alloy (NiCo, NiMn, and NiCu) embedded CNTs can also be achieved, though further material optimization is still underway (Experimental section, Fig. S8-S12). The Raman spectrum of NiFe@CNTs reflects the characteristic *D* band (1376 cm⁻¹), *G* band (1585 cm⁻¹), and the broad *2D* band (2870 cm⁻¹) from the N-doped multi-walled CNTs with few wrinkled graphene layers (Fig. S13) [7]. Compared to Ni@CNTs (0.93), the higher *I_D*/*I_G* ratio of 1.03 and the red shift in the *2D* band of NiFe@CNTs imply more disordered edge defects and a higher degree of structural defects in the carbon lattices, thus exhibiting better electroactivity toward oxygen catalysis with the introduction of Fe [39, 40]. In light of its simplicity, versatility, and scale-up capability, this

wet-electrochemistry-assisted synthetic strategy is suitable for building high-quality, self-supporting transition metal/alloy@CNTs catalysts.

X-ray photoelectron spectroscopy (XPS) was performed to further analyze the catalyst surface and chemical states. A full-scan spectrum of the corresponding catalyst confirms the presence of all the expected elements (Fig. S14a-c). The N 1s spectra of Ni@CNTs and NiFe@CNTs exhibit four peaks attributed to pyridinic-nitrogen (398.20 eV), graphitic-nitrogen (400.93 eV), NO_x (404.00 eV), and metal-nitrogen (M–N_x, 398.97 eV), respectively. (Fig. S14d). The addition of Fe is observed to increase the pyridinic-nitrogen content from 20.8% for Ni@CNTs to 27.8% for NiFe@CNTs, and the M–N_x content increased from 39.8 to 45.9%, correspondingly. Generally, pyridinic-nitrogen assists in anchoring metal sites and forming thermodynamically stable M–N_x bonds, often serving as active sites during ORR [23]. In the Ni 2p spectra, the three sets of featured peaks correspond to the metallic Ni⁰ (853.00 eV, 871.41 eV), Ni²⁺ (855.35 eV, 873.35 eV), and Ni³⁺ (856.92 eV, 875.33 eV), respectively (Fig. 1h). Compared to NiFe, the average valence states of nickel in Ni@CNTs and NiFe@CNTs are decreased due to an increased content of Ni⁰ and Ni²⁺, along with decreased Ni³⁺ species. Three pairs of distinct peaks in the Fe 2p spectra are attributed to the Fe⁰ (706.20 eV, 721.70 eV), Fe²⁺ (711.39 eV, 724.64 eV), and Fe³⁺ (714.18 eV, 727.65 eV), separately (Fig. 1i). NiFe@CNTs exhibit a higher content of Fe²⁺ as compared to NiFe. Notably, the nickel (Ni²⁺, Ni³⁺) and iron (Fe²⁺, Fe³⁺) peaks with higher oxidation states positively shift towards lower binding energies. This may be associated with the charge transfer from the N-doped CNT matrix to NiFe alloy through strong M–N_x interactions [41, 42]. Furthermore, both Ni²⁺ and Ni³⁺ in NiFe@CNTs shift by approximately 0.1 eV to higher binding energy compared with Ni@CNTs. This implies electron transfer from Ni to Fe, enhancing synergistic electronic interactions within the bimetallic NiFe alloys, thereby effectively regulating the electronic states of single-metal atomic sites towards improved OER and ORR performance [43, 44].

Figure 2a shows the electron paramagnetic resonance (EPR) spectra of NiFe@CNTs and Ni@CNTs under a low temperature of 77 K. The intensity of Lorentz lines is positively correlated with the number of unpaired electrons. NiFe@CNTs exhibit a stronger signal than Ni@CNTs, suggesting that NiFe@CNTs contain more unpaired electrons and a distinctly coordination-unsaturated local environment [45, 46]. Furthermore, we simulated the local electronic states of NiFe@CNTs to gain an in-depth understanding of the charge transfer between the components. The electron-transfer behavior is elucidated by the first principles differential charge calculation, where the yellow (red) and cyan (blue) pieces represent the electron-accumulation and electron-deficient regions, respectively. As shown in Fig. 2b–d,

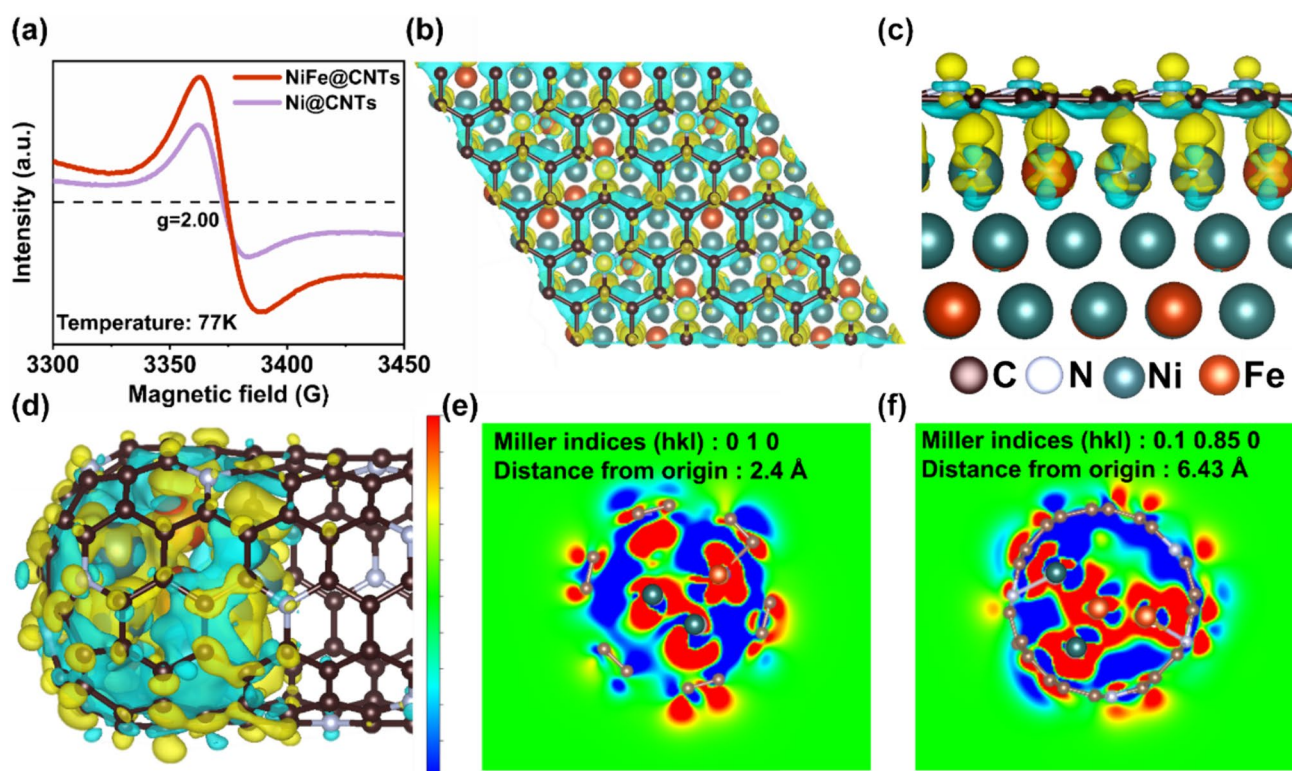


Fig. 2 **a** Low-temperature EPR spectra of NiFe@CNTs and Ni@CNTs. **b–d** 3D electron density difference of NiFe-NC in NiFe@CNTs (The yellow color represents the electron-accumulation area while the blue color represents the electron-deficient area. The balls

with brown, white, green, and orange are C, N, Ni and Fe, respectively). **e, f** Isosurface of differential charge density: 2D slices of charge density distribution

the 3D charge-density difference reveals the charge transfer from the NiFe alloys to the N-doped carbon, accumulating at the electronegative nitrogen over the carbon layer surface. Previous studies indicate that such electron-rich N-doped carbon surfaces are advantageous for catalytic performance [47, 48]. Figure 2e and f displays the corresponding 2D slice of the charge-density distribution for NiFe-NC in NiFe@CNTs. Due to the electronegativity difference between the metals and nitrogen atoms, frequent electron exchange occurs between NiFe and the N-doped CNTs. This result is reasonable as delocalized π electrons surrounding the highly curved CNT tips could easily transfer and alter the d -band center of the closely contacted metal species, ultimately modulating the surface electronic structure of the tip-enriched NiFe alloys@CNTs for increased electrochemical reactivity [38].

2.2 Electrochemical Performance of Bifunctional Oxygen Electrodes

A typical three-electrode system was employed to assess the electrochemical activities of catalysts towards bifunctional oxygen catalysis. The as-obtained self-supported

catalysts directly served as the working electrode without any additional current collectors or additives. Unless otherwise stated, the standard hydrogen electrode (RHE) potential was used for the reference potentials mentioned. As shown in Fig. 3a, NiFe@CNTs exhibit a remarkably low overpotential of 220 mV at a current density of 10 mA cm^{-2} ($E_{j=10} = 1.45 \text{ V}$), significantly smaller than that of RuO_2 (280 mV), NiFe (260 mV), Ni@CNTs (225 mV), and the CNTs counterpart (290 mV), which was prepared by post acid-etching of NiFe@CNTs to remove the metallic components, respectively. Additionally, NiFe@CNTs demonstrate a low overpotential of 395 mV to achieve a high current density of 100 mA cm^{-2} . The superior OER kinetics on the surface of NiFe@CNTs is further evidenced by its low Tafel slope (93.1 mV dec^{-1}), lower than that of RuO_2 ($165.4 \text{ mV dec}^{-1}$), NiFe ($193.1 \text{ mV dec}^{-1}$), Ni@CNTs ($326.0 \text{ mV dec}^{-1}$), and CNTs ($183.6 \text{ mV dec}^{-1}$), respectively (Fig. 3b). Accordingly, the derived electrochemically active surface area (ECSA) of NiFe@CNTs (86.20 mF cm^{-2}) distinctly surpasses that of NiFe-N@CNTs (75.52 mF cm^{-2}), and is several times higher than that of Ni@CNTs (21.75 mF cm^{-2}) and NiFe (6.45 mF cm^{-2}) (Fig. S15a–e). The increased ECSA of NiFe@CNTs is synergistically

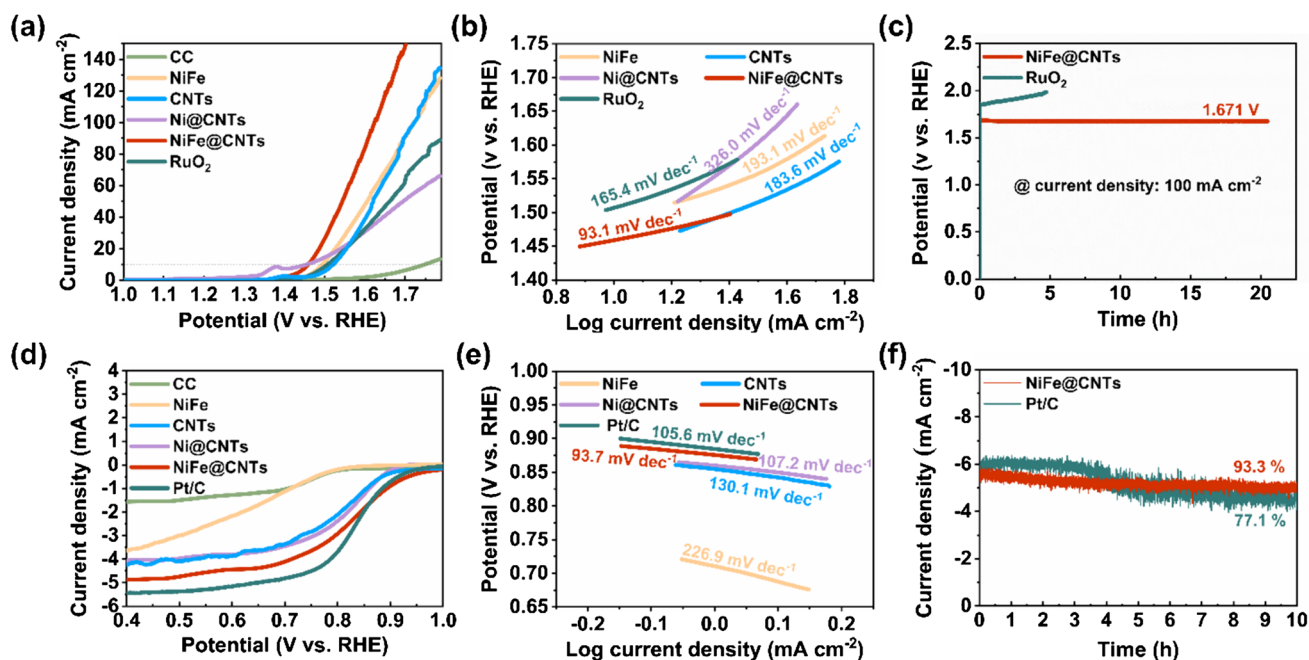


Fig. 3 a OER polarization curves in 1 M KOH. b OER Tafel plots. c Chronopotentiometric responses of NiFe@CNTs and RuO₂ at 100 mA cm⁻². d ORR polarization curves in O₂ saturated 0.1 M

KOH. e ORR Tafel plots. f Chronoamperometric measurements of NiFe@CNTs and Pt/C at constant potential (0.5 V vs. RHE)

contributed by three factors. Firstly, tip-enriched bimetallic alloys in ordered CNTs can provide more accessible active sites. Secondly, bamboo-like CNT arrays being rooted on porous and 3D conductive CC substrate are conferred with high specific surface area, and shortened pathways for directed electron transfer and ion diffusion, thus facilitating the exposure of active sites [30]. Thirdly, the involvement of suitable Fe favors the bimetallic effect, between Ni and Fe species, leading to easier electronic interactions between the metal sites and the N-doped carbon possessing abundant edge defects for improved electroactivity [16]. To evaluate the long-term OER stability, NiFe@CNTs were tested under a high current density of 100 mA cm⁻² and it maintained at a potential of 1.67 V after 20 h (Fig. 3c). In contrast, the RuO₂ electrode exhibited an obvious decay tendency during the first 5 h. Nyquist plots of NiFe@CNTs also indicate increased OER electroactivity with extremely low interfacial charge-transfer resistance compared to other electrodes (Fig. S16a).

The ORR electrocatalytic activity of the catalysts was measured in an oxygen-saturated 0.1 M KOH solution. Figure 3d presents the LSV curves of the electrodes for ORR. NiFe@CNTs exhibit an onset potential of 0.95 V, outperforming NiFe, Ni@CNTs, CNTs, and Pt/C, respectively. Additionally, NiFe@CNTs achieved an impressive half-wave potential ($E_{1/2}$) of 0.82 V and an acceptable ultimate diffusion current density, close to the Pt/C benchmark. The electrochemical impedance spectroscopy (EIS) curve of

NiFe@CNTs further indicates its favorable charge-transfer resistance at the electrode/electrolyte interface (Fig. S16b), shedding light on the comparable intrinsic catalytic activity to the Pt/C counterpart. Figure 3e shows that NiFe@CNTs have a Tafel slope of 93.7 mV dec⁻¹, which is lower than the other contrast electrodes, reflecting the accelerated interfacial kinetics of NiFe@CNTs toward the ORR process. When operating at a constant potential of 0.5 V, NiFe@CNTs can maintain its electroactivity well with higher current retention of 93.3% than that of Pt/C (77.1%) after 10 h (Fig. 3f). Compared to recently reported high-efficiency bifunctional oxygen catalysts based on bimetal hybrids, our self-supported NiFe@CNTs catalyst still stands out with prominent OER/ORR bifunctionality (Table S3). Particularly, we have investigated the morphology and composition variation of the self-supported electrocatalyst after prolonged OER/ORR processes. SEM images of NiFe@CNTs reveal the inevitable carbon corrosion/oxidation of several highly active CNTs and particle coarsening over the catalyst surfaces during high-voltage reaction conditions, along with increased exposure of the active sites from the bimetallic nanoalloys, though the pristine nanostructure of NPs-embedded CNTs can be roughly sustained (Fig. S17a, b). This phenomenon can be further inferred by the significantly decreased strength of the carbon peak accompanied by more pronounced characteristic peaks of the NiFe alloys for NiFe@CNTs after OER and ORR tests (Fig. S18). Nevertheless, the fundamental chemical composition of NiFe@CNTs was well

preserved to demonstrate its exceptional operational stability upon continuous oxygen catalysis. Additionally, the OER/ORR performance of the set of similarly-prepared catalysts, *i.e.*, Ni@CNTs, NiCo@CNTs, NiMn@CNTs, and NiCu@CNTs, were studied without further optimization (Fig. S19a, b). Preliminary results show that NiMn@CNTs exhibited low OER overpotentials while NiCo@CNTs obtained considerable ORR activity.

Density functional theory (DFT) computations were employed to interpret the catalytic kinetics of Ni@CNTs and NiFe@CNTs. Ideally, the OER/ORR process follows a four-electron transfer reaction pathway [10, 49]. The aforementioned results hint at the key role of the NiFe alloy in the improved bifunctional catalytic process. To clarify the contribution of exact active sites in the hybrid catalyst, four local configuration models of NiFe@CNTs were rationally established and optimized (Fig. S20a-c). Specifically, NiFe-NC (NiFe) represents the bimetallic NiFe active sites bridging with the edges of N-doped CNTs (Fig. 4a), NiFe-NC (NC) describes the active sites of N-doped carbon bridging the top NiFe alloys (Fig. 4b), Ni-Fe represents the isolated NiFe clusters serving as active sites near the top CNTs (Fig. 4c), and N-C (C) is the N-doped CNT sites that don't interact with metals (Fig. 4d). For comparison, Ni-NC (Ni), Ni-NC (NC), and Ni sites without Fe participation were also discussed (Fig. S21a-c). Figure 4e demonstrates the calculated free energy diagrams of diverse oxo-intermediates (OH^* , O^* , and OOH^*) adsorbed on the surface of different active sites for OER [47]. The conversion between OOH^* and O_2 is the rate-determining step (RDS) for NiFe-NC (NiFe), Ni-NC (Ni), Ni-Fe, and Ni, with an energy barrier of 0.52 eV, 0.62 eV, 0.44 eV, and 0.82 eV, respectively. However, as for NiFe-NC (NC), Ni-NC (NC), and N-C (C), the conversion between O^* and OOH^* became the RDS due to the unique surface structure and modulation of N-doped CNTs [50]. OER and ORR are chemically inverse reactions [51, 52]. During the ORR pathway in Fig. 4f, the free energy of the rate-determining step (RDS) exhibits an increasing order as follows: NiFe-NC (NC) (0.11 eV) < Ni (0.36 eV) < NiFe-NC (NiFe) (0.44 eV) < Ni-NC (NC) (0.52 eV) < Ni-Fe (0.57 eV) < Ni-NC (Ni) (0.65 eV) < N-C (NC) (0.67 eV). (Fig. S20-23 Table S4, 5). These results prove the positive effect of Fe incorporation to fulfill bimetallic synergistic interaction and remarkably reduce energy barriers for NiFe@CNTs, which benefits optimized adsorption of intermediates by the diatomic active sites, accelerating the OER/ORR kinetics [16]. Figure 4g summarizes the free energy profiles of the four different catalytic sites in NiFe@CNTs. Under the alkaline condition of 1.23 V, the adsorption/desorption of intermediates on the surface of NiFe-NC (NC) is more thermodynamically favorable by lowered energy barriers, thus dominantly contributing to improved OER/ORR kinetics. This finding accords well

with the latest research indicating that porous carbon support with highly curved surfaces can efficiently tune the local coordination environment and electronic structure of the metal sites for appropriate adsorption of O-containing intermediates [35]. Synergistically, NiFe-NC (NiFe), Ni-Fe, and N-C (C) can also enable more exposed active sites for intermediates binding, giving rise to dramatically enhanced intrinsic activities of the integrated NiFe@CNTs catalyst.

2.3 Electrochemical Performance of Aqueous ZABs

Contact angle (CA) tests were conducted on the catalysts. NiFe exhibits high hydrophobicity with a CA of 134° due to the poor affinity between the nonpolar metallic nanoalloys and the polar water molecules (Fig. S24a-c). After the formation of NiFe@CNTs, the catalyst surfaces become extremely hydrophilic with a CA of 50° , facilitating the penetration of the alkaline electrolyte. Interestingly, we etched the NiFe NPs on the top of NiFe@CNTs by acid treatment and found that the post-treated CNTs showed hydrophobic surfaces with poor infiltration ability of OH^- and H_2O species. This indicates that tip-enriched NiFe NPs significantly regulate the hydrophilic-phobic microenvironment at the catalyst/electrolyte interfaces through the unique pore structure and surface reconstruction of the highly curved CNTs matrix by interacting with metal-N species [30, 35, 53, 54]. Furthermore, molecular dynamics (MD) simulations were employed to study the diffusion distribution of oxygen and water molecules over the NiFe@CNTs catalyst surfaces. Two optimized structural models of tip-enriched NiFe@CNTs and middle-dispersed NiFe@CNTs were analyzed under actual battery reaction conditions, using 6 M KOH as the electrolyte and applying an external potential of 1.5 V to the environment. Figure 5a and b depicts the time-dependent distribution of $\text{H}_2\text{O}/\text{OH}^-$ and O_2 over the two catalyst models. From 0 to 10 ns, most of the O_2 molecules gradually penetrated the CNTs and stayed between the metal alloys, while most of the $\text{H}_2\text{O}/\text{OH}^-$ species tended to gather and distribute on the top of CNTs. For tip-enriched NiFe@CNTs, a small amount of $\text{H}_2\text{O}/\text{OH}^-$ could permeate into and further stay near the top of CNTs due to the hydrophilicity of NiFe@CNTs. The statistical distributions of H_2O and O_2 are shown in Fig. 5c. Both H_2O and O_2 species were concentrated at 0.7–1.0 along the Z axis, *i.e.*, close to the apical NiFe alloys of tip-enriched NiFe@CNTs. In contrast, for middle-dispersed NiFe@CNTs, H_2O was concentrated at 0.7–0.9 along the Z axis (near the top CNTs), while O_2 was concentrated at 0.4–0.6 along the Z axis (near the middle NiFe alloys). These results unveil that tip-enriched bimetallic nanoalloys optimize the local gas/liquid environment of NiFe@CNTs, favoring accelerated diffusion/adsorption of the OH^-/O_2 reactants within a more balanced three-phase

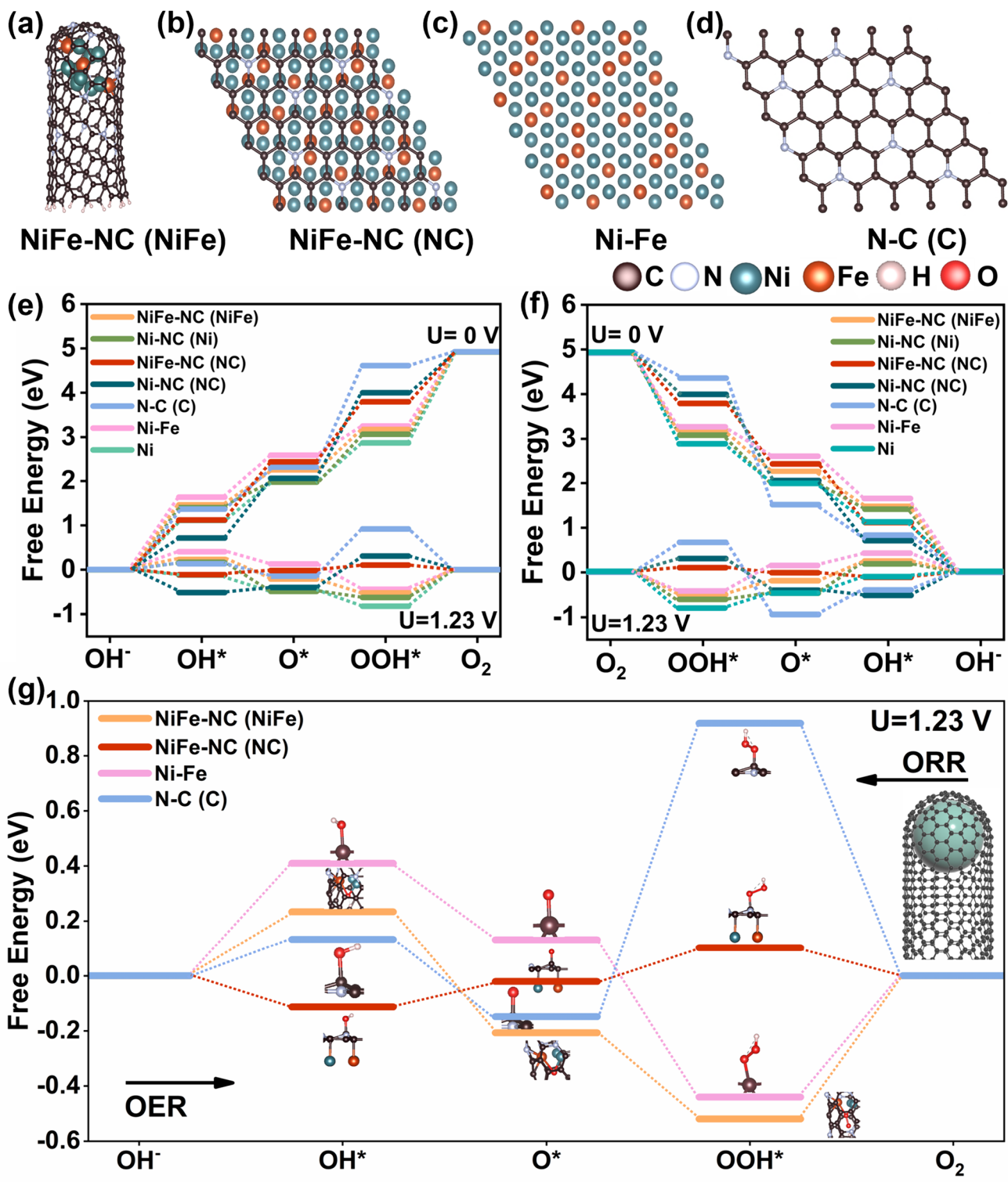


Fig. 4 Different adsorption sites of optimized configurations for NiFe@CNTs. **a** NiFe-NC (NiFe). **b** NiFe-NC (NC). **c** Ni-Fe. **d** N-C (C). Free energy diagrams of diverse oxointermediates (OH*, O* and OOH*) on the surface of NiFe-NC (NiFe), NiFe-NC (NC), Ni-

Fe, Ni-NC (Ni), Ni-NC (NC), Ni and N-C (C) sites for **e** OER and **f** ORR, respectively. **g** Free energy diagrams of different intermediates adsorbed on the surface of NiFe-NC (NiFe), NiFe-NC (NC), Ni-Fe and N-C (C) for NiFe@CNTs at U=1.23 V

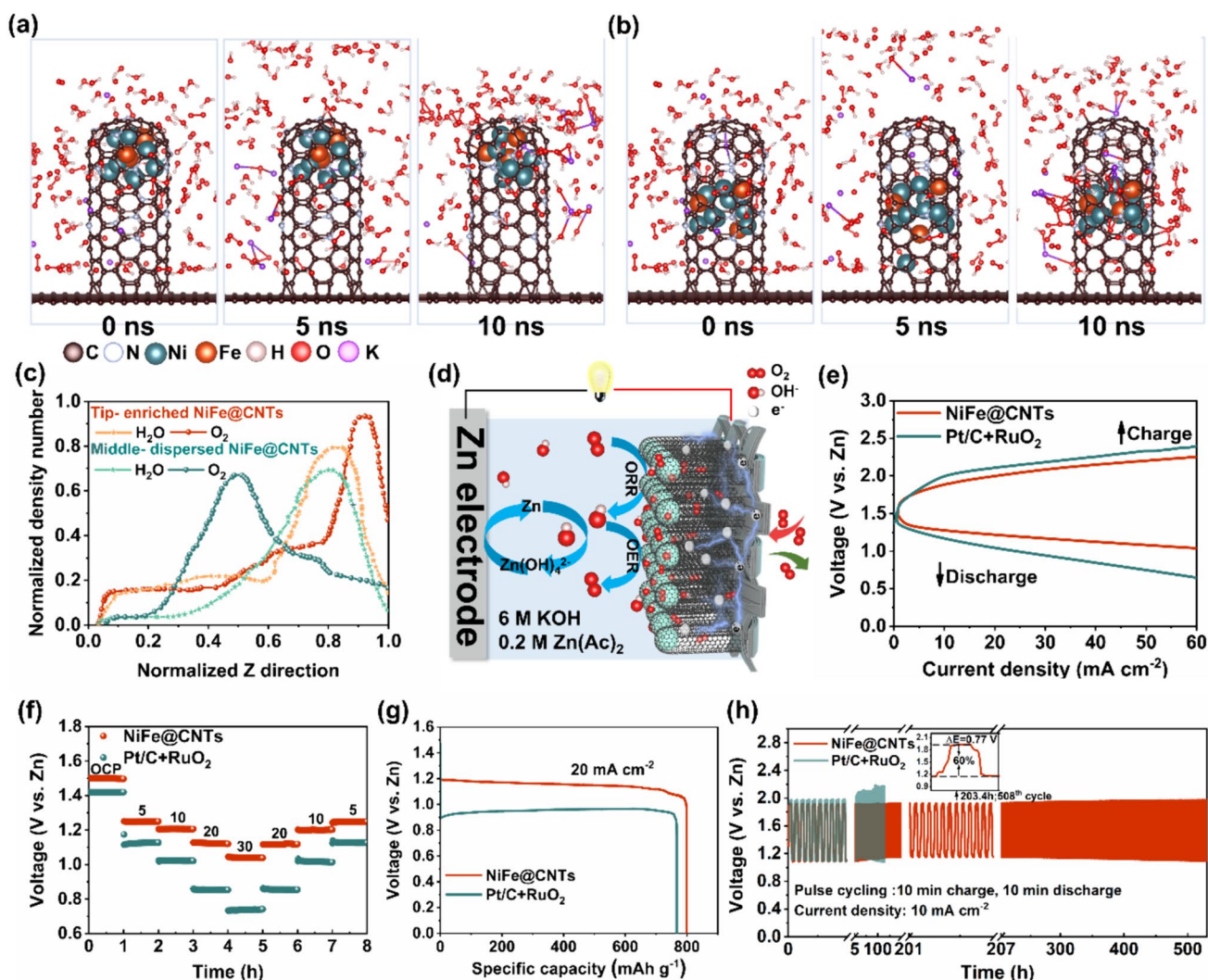


Fig. 5 Molecular dynamics simulation of O_2 and H_2O diffusion behavior under alkaline conditions. Optimized structural model of NiFe@CNTs with **a** tip-enriched NiFe@CNTs or **b** middle-dispersed NiFe@CNTs, respectively. **c** Average density of O_2 and H_2O molecules along the Z-direction of the two NiFe@CNTs models (from bottom to top in the simulation box). **d** Schematic diagram of an aqueous ZAB based on a self-supporting NiFe@CNTs air cathode.

(catalyst-electrolyte-oxygen) reaction microinterfaces for boosted oxygen catalytic kinetics.

The actual bifunctional oxygen catalytic activities of NiFe@CNTs were assessed in aqueous ZABs. The structural diagram of an alkaline rechargeable ZAB is depicted in Fig. 5d, where the self-supported NiFe@CNTs catalyst serves as the air cathode, and a polished zinc sheet functions as the anode. For comparison, ZABs based on commercial Pt/C + RuO₂ catalysts were also investigated. Due to the excellent OER/ORR activities of the bifunctional cathode, the NiFe@CNTs battery displays significantly reduced charge/discharge overpotentials compared to the Pt/C + RuO₂ counterpart under all current densities (Fig. 5e).

e Charge/discharge polarization curves. **f** Discharge curves of different ZABs at various current densities (5, 10, 20, and 30 mA cm⁻²). **g** Constant current cyclic discharge capacity curves of ZABs at 20 mA cm⁻². **h** Long-term cyclic stability of NiFe@CNTs and Pt/C + RuO₂ ZABs at 10 mA cm⁻². Inset: the enlarged charge/discharge voltage profiles for the 508th cycle

The NiFe@CNTs battery achieves a high open-circuit voltage (V_{oc}) of up to 1.53 V and a peak power density of 109 mW cm⁻², outperforming the Pt/C + RuO₂ battery, which shows a V_{oc} of 1.48 V and a peak power density of 93 mW cm⁻² (Fig. S25a, b). Figure 5f illustrates the voltage plateaus of ZABs at various discharge currents of 5, 10, 20, and 30 mA cm⁻², respectively. NiFe@CNTs maintains a high voltage plateau with a slower voltage loss rate than that of Pt/C + RuO₂ as the discharge current gradually increases, demonstrating impressive rate capability even under a high current density of 30 mA cm⁻². Additionally, the discharge voltage recovers well when the current density is reversed back to 5 mA cm⁻². At a current density of 20 mA cm⁻²,

the specific discharge capacity of the NiFe@CNTs battery is 800 mAh g^{-1} (normalized to the mass of consumed zinc), higher than that of the Pt/C + RuO₂-based battery (768 mAh g^{-1}), and the former exhibits a high gravimetric energy output of $936 \text{ Wh kg}_{\text{Zn}}^{-1}$ (Fig. 5g).

As shown in Fig. 5h, after 520 h cycling (1581 charge/discharge cycles) at 10 mA cm^{-2} , the NiFe@CNTs battery exhibits outstanding cyclic stability, maintaining a charge/discharge voltage difference (ΔE) of just 0.77 V at the 508th cycle (corresponds to a round-trip efficiency of 60%). This performance significantly outperforms the Pt/C + RuO₂ battery, which exhibited noticeable performance degradation with increasing charge voltages and decreasing discharge voltages even within the first 100 h. The excellent cycling performance of the NiFe@CNTs battery was further confirmed by charging/discharging at 20 mA cm^{-2} , achieving low charge/discharge gaps and round-trip efficiencies of 54–56% over 425 h/1065 cycles (Fig. S26). The battery performance of NiFe@CNTs-based ZABs was also compared with recently reported analogs (Table S6), confirming the superior bifunctional oxygen activities and practical potential of NiFe@CNTs for enhanced ZABs. The morphology and composition evolution of the NiFe@CNTs cathode after extended battery cycling (80 h/200 cycles) at 20 mA cm^{-2} were further investigated. According to the morphological and compositional characterizations after cycling, the original nanoarray structure and basic chemical composition of NiFe-embedded CNTs can be recognized and maintained (Fig. S27 a-c, Fig. S28a, b). However, the cathode surface showed noticeable coverage by rough discharge products, likely amorphous ZnO deposits inevitably resulting from constrained oxygen catalytic reactions during continuous battery charge/discharge processes [4]. Moreover, initial Ni⁰ species were completely depleted, accompanied by a significant increase in the ratio of Fe³⁺ and dominant M–H₂O/M–OH peaks in the cycled NiFe@CNTs cathode (Fig. S29a-f). These changes are associated with the formation of high-valent metal hydroxide intermediates during prolonged OER/ORR processes [55]. Moreover, tip-embedded NiFe bimetals in N-doped CNTs can be well preserved after battery cycling (Fig. S30a-e), further confirming the superior mechanical and electrochemical tolerance of the cathode catalyst.

2.4 Performance of All-Solid-State Flexible ZABs

To examine the practical applicability of self-supporting catalysts for flexible/wearable batteries [56, 57], the as-prepared NiFe@CNTs cathode was directly integrated into flexible ZABs by using quasi-solid-state gel electrolyte, as schematically presented in Fig. 6a. The thin solid-state battery exhibited a V_{oc} of 1.52 V , and an encouraging peak power density of 108 mW cm^{-2} , outperforming the Pt/C + RuO₂ battery

(Fig. 6b, c). At a discharge current of 5 mA cm^{-2} , the NiFe@CNTs-based flexible ZAB achieved a specific capacity of $829 \text{ mAh g}_{\text{Zn}}^{-1}$ (gravimetric energy density: $1003 \text{ Wh kg}_{\text{Zn}}^{-1}$), while maintaining a specific capacity of $769 \text{ mAh g}_{\text{Zn}}^{-1}$ can still be gained at an increased current of 20 mA cm^{-2} (Fig. S31a). As depicted in Fig. 6d, the NiFe@CNTs-based battery exhibited a small charge–discharge voltage gap of 0.77 V at a constant current of 2 mA cm^{-2} and remained stable over 24-h cycling, whereas the battery utilizing commercial Pt/C + RuO₂ catalysts only lasted for 16 h. Upon increasing the current density from 5 to 50 mA cm^{-2} , the discharge voltage plateau decreased from 1.27 to 1.08 V , but smoothly returned to 1.27 V as the current reverted to 5 mA cm^{-2} (Fig. S31b), showing high energy output, exceptional rate capabilities, and reversible durability of our flexible battery (Table S6).

With delight, we further evaluated the superior electrochemical performance of solid-state flexible ZABs under varied device connections to meet integrated application requirements. As shown in Fig. 6e, when two flexible batteries are connected in parallel, the charge/discharge gap equals that of an individual battery and is nearly half of that of two batteries connected in series, aligning well with the expected resistances for flexible batteries through different connections (Fig. S32). Therefore, NiFe@CNTs-based flexible ZABs can achieve any desired voltage/energy output by connecting them in series or parallel (Fig. S33a-c). Despite being subjected to various external stresses, the flexible ZAB can still withstand mechanical deformation and operate stably, as evidenced by the largely unaffected charge/discharge profiles at different bending angles (0° , 90° , 120° , 180°) under 2 mA cm^{-2} (Fig. 6f). Furthermore, the discharge performance of the flexible battery remains consistent after uninterrupted bending cycles at a 90° angle (Fig. 6g). Even after 1000 cycles of bending, the discharge plateau only decays by 30 mV compared to the initial voltage, showcasing the remarkable mechanical flexibility and high bending strength of the flexible ZABs. Figure 6h demonstrates the practical potential of our flexible ZABs as miniaturized or portable power supplies for various applications (Video S1). Encouragingly, three combined flexible ZABs can steadily charge a smartphone, while two batteries connected in series can illuminate and continuously power a homemade LED board comprising 45 commercial LEDs under diverse bending conditions. All the above results signify the high specific power/energy density, superior cyclic stability, and impressive mechanical performance of NiFe@CNTs-based ZABs for flexible/wearable energy storage.

3 Conclusions

In summary, we propose tip-enriched NiFe nanoalloys encapsulated in N-doped CNT arrays as binder-free bifunctional oxygen catalysts. Utilizing a straightforward

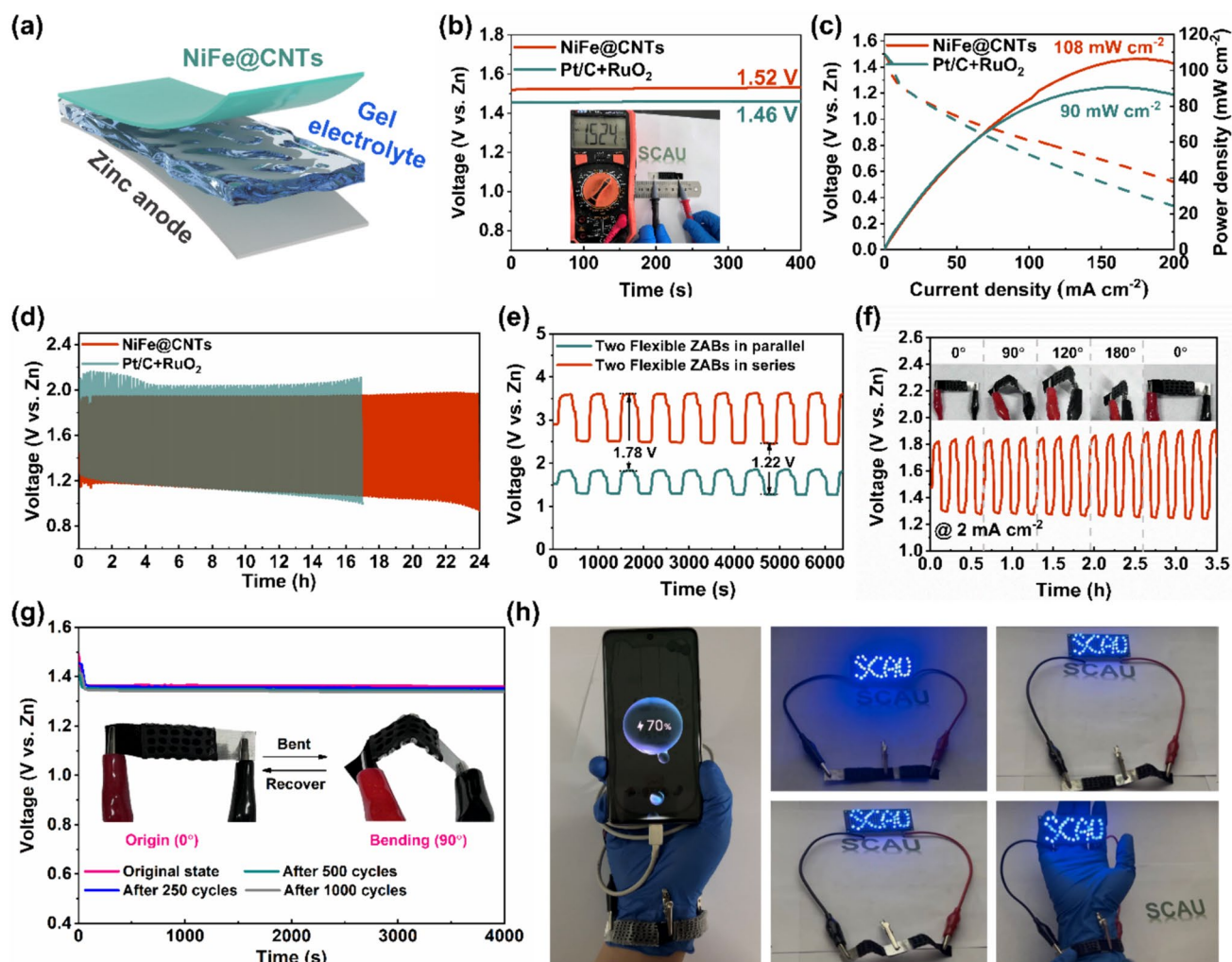


Fig. 6 Performances of solid-state flexible ZABs. **a** Schematic diagram of a solid-state flexible rechargeable ZAB based on NiFe@CNTs air cathode. **b** Open circuit potentials; the plug-in illustration displays the stable voltage provided by the NiFe@CNTs-based flexible ZAB. **c** Discharge polarization curves and the corresponding power density curves. **d** Charge/discharge cyclic curves at a constant current density of 2 mA cm^{-2} . **e** Charging and discharging curves of

two flexible ZABs in series and in parallel combinations, respectively. **f** Charge and discharge curves of the flexible battery at different bending angles. **g** The voltage curves of flexible ZAB bent at 90° and recovered for different numbers of cycles (250, 500, 1000 cycles). **h** Flexible ZABs charge a mobile phone (left) and drive the LED screen under different bent conditions

wet-electrochemistry mediated synthetic approach, we fabricate well-constructed NiFe@CNTs with a 3D porous heterostructure and good electrical conductivity guarantee, ensuring efficient electrolyte infiltration and charge transport for enhanced oxygen catalysis on the catalyst surface. Crucially, both experimental and DFT calculations elucidate that dispersed NiFe nanoalloys with a synergistic bimetallic effect enrich the accessible active sites at the top of CNTs, thereby modulating the electronic interaction between the M-N_x moieties and the defect-rich CNT matrix to reduce the energy barrier of intermediates adsorption and promote redox kinetics. MD simulation results further reveal that NiFe@CNTs possess more balanced triphase interfaces, facilitating favorable

O_2 diffusion and $\text{H}_2\text{O}/\text{OH}^-$ permeation. These advantages synergistically contribute to the superior bifunctionality of NiFe@CNTs, leading to remarkably lowered OER and ORR overpotentials. As a result, rechargeable aqueous ZABs based on NiFe@CNTs cathodes achieve high gravimetric energy, long cycling life, and high rate capability. Furthermore, monolithic NiFe@CNTs demonstrate impressive electrochemical performance and superb mechanical flexibility. Making them highly suitable for high-performance solid-stated ZABs. This study provides a convenient and scalable approach to constructing efficient and binder-free M-N-C catalysts for multifunctional catalysis and flexible/wearable batteries.

Supplementary Information The online version contains supplementary material available at <https://doi.org/10.1007/s42765-024-00425-5>.

Acknowledgements This research was financially supported by the Natural Science Foundation of Guangdong Province (No. 2023A1515030131; 2022A1515010476), and the National Natural Science Foundation of China (22078118).

Data availability All the data in this manuscript can be reproduced for these findings. We should apologize that the raw processed data cannot be shared at this time in consideration of ongoing research.

Declarations

Conflicts of interest The authors declare that there is no conflict of interest.

References

- Fu J, Cano ZP, Park MG, Yu A, Fowler M, Chen Z. Electrically rechargeable zinc-air batteries: progress, challenges, and perspectives. *Adv Mater.* **2017**;29(7):1604685.
- Wang Q, Kaushik S, Xiao X, Xu Q. Sustainable zinc-air battery chemistry: advances, challenges and prospects. *Chem Soc Rev.* **2023**;52(17):6139–90.
- Jiao ML, Zhang Q, Ye CL, Gao RH, Dai LX, Zhou GM, Cheng HM. Isolating contiguous Fe atoms by forming a Co–Fe intermetallic catalyst from spent lithium-ion batteries to regulate activity for zinc–air batteries. *ACS Nano.* **2022**;16:13223–31.
- Kuang J, Shen Y, Zhang Y, Yao J, Du J, Yang S, Zhang S, Fang Y, Cai X. Synergistic bimetallic CoCu-codecorated carbon nanosheet arrays as integrated bifunctional cathodes for high-performance rechargeable/flexible zinc-air batteries. *Small.* **2023**;19(17): e2207413.
- Zhong X, Shao Y, Chen B, Li C, Sheng J, Xiao X, Xu B, Li J, Cheng HM, Zhou G. Rechargeable zinc–air batteries with an ultralarge discharge capacity per cycle and an ultralong cycle life. *Adv Mater.* **2023**;35(30): e2301952.
- Jiao ML, Zhang Q, Ye CL, Liu ZB, Zhong XW, Wang JX, Li C, Dai LX, Zhou GM, Cheng HM. Recycling spent LiNi_{1-x}–yMn_x–Co_yO₂ cathodes to bifunctional NiMnCo catalysts for zinc–air batteries. *Proc Natl Acad Sci.* **2022**;119(20): e2202202119.
- Ye D, Shen Y, Mao H, Liang Y, Gao Q, Yang S, Zhang S, Cai X, Fang Y. Dual-sources directed construction of N-doped carbon nanotube arrays as superior self-supported bifunctional air electrodes for rechargeable/flexible zinc-air batteries. *Chem Eng J.* **2023**;464: 142601.
- Wu M, Zhang G, Chen N, Chen W, Qiao J, Sun S. A self-supported electrode as a high-performance binder- and carbon-free cathode for rechargeable hybrid zinc batteries. *Energy Storage Mater.* **2020**;24:272–80.
- Guan C, Sumboja A, Zang W, Qian Y, Zhang H, Liu X, Liu Z, Zhao D, Pennycook SJ, Wang J. Decorating Co/CoN_x nanoparticles in nitrogen-doped carbon nanoarrays for flexible and rechargeable zinc-air batteries. *Energy Storage Mater.* **2019**;16:243–50.
- Yang X, Zhou Z, Zou Y, Kuang J, Ye D, Zhang S, Gao Q, Yang S, Cai X, Fang Y. Interface reinforced 2D/2D heterostructure of Cu–Co oxides/FeCo hydroxides as monolithic multifunctional catalysts for rechargeable/flexible zinc-air batteries and self-powered water splitting. *Appl Catal B.* **2023**;325:122332.
- Zhang Y, Deng YP, Wang J, Jiang Y, Cui G, Shui L, Yu A, Wang X, Chen Z. Recent progress on flexible Zn–air batteries. *Energy Storage Mater.* **2021**;35:538–49.
- Lu X, Yang P, Wan Y, Zhang H, Xu H, Xiao L, Li R, Li Y, Zhang J, An M. Active site engineering toward atomically dispersed M–N–C catalysts for oxygen reduction reaction. *Coord Chem Rev.* **2023**;495: 215400.
- Hao YN, Hu F, Chen Y, Wang YH, Xue JJ, Yang SY, Peng SJ. Recent progress of electrospun nanofibers for zinc–air batteries. *Adv Fiber Mater.* **2022**;4:185–202.
- Xu H, Wang D, Yang P, Liu A, Li R, Li Y, Xiao L, Ren X, Zhang J, An M. Atomically dispersed M–N–C catalysts for the oxygen reduction reaction. *J Mater Chem A.* **2020**;8(44):23187–201.
- Huang Y, Chen Y, Xu M, Ly A, Gili A, Murphy E, Asset T, Liu Y, De Andrade V, Segre CU, et al. Catalysts by pyrolysis: transforming metal-organic frameworks (MOFs) precursors into metal–nitrogen–carbon (M–N–C) materials. *Mater Today.* **2023**;69:66–78.
- Jing Q, Mei Z, Sheng X, Zou X, Yang Y, Zhang C, Wang L, Sun Y, Duan L, Guo H. 3d orbital electron engineering in oxygen electrocatalyst for zinc-air batteries. *Chem Eng J.* **2023**;462: 142321.
- Kim J, Yoo JM, Lee HS, Sung YE, Hyeon T. Single-atom M–N–C catalysts for oxygen reduction electrocatalysis. *Trends Chem.* **2021**;3(9):779–94.
- Song JN, Chen Y, Huang HJ, Wang JJ, Huang SC, Liao YF, Fetohi AF, Hu F, Chen HY, Li LL, Han XP, El-Khatib KM, Peng SJ. Heterointerface engineering of hierarchically assembling layered double hydroxides on cobalt selenide as efficient trifunctional electrocatalysts for water splitting and zinc–air battery. *Adv Sci.* **2022**;9:2104522.
- Miao Z, Wang X, Zhao Z, Zuo W, Chen S, Li Z, He Y, Liang J, Ma F, Wang HL, et al. Improving the stability of non-noble-metal M–N–C catalysts for proton-exchange-membrane fuel cells through M–N bond length and coordination regulation. *Adv Mater.* **2021**;33(39): e2006613.
- Tang T, Wang Z, Guan J. Optimizing the electrocatalytic selectivity of carbon dioxide reduction reaction by regulating the electronic structure of single-atom M–N–C materials. *Adv Funct Mater.* **2022**;32(19):2111504.
- He Y, Yang X, Li Y, Liu L, Guo S, Shu C, Liu F, Liu Y, Tan Q, Wu G. Atomically dispersed Fe–Co dual metal sites as bifunctional oxygen electrocatalysts for rechargeable and flexible Zn–air batteries. *ACS Catal.* **2022**;12(2):1216–27.
- Hu J, Zhang C, Sun M, Qi Q, Luo S, Song H, Xiao J, Huang B, Leung MKH, Zhang Y. Ultrastable bimetallic Fe₂Mo for efficient oxygen reduction reaction in pH-universal applications. *Nano Res.* **2022**;15(6):4950–7.
- Li Y, Shan W, Zachman MJ, Wang M, Hwang S, Tabassum H, Yang J, Yang X, Karakalos S, Feng Z, et al. Atomically dispersed dual-metal site catalysts for enhanced CO₂ reduction: mechanistic insight into active site structures. *Angew Chem Int Ed.* **2022**;61(28): e202205632.
- Xiao M, Chen Y, Zhu J, Zhang H, Zhao X, Gao L, Wang X, Zhao J, Ge J, Jiang Z, et al. Climbing the apex of the ORR volcano plot via binuclear site construction: electronic and geometric engineering. *J Am Chem Soc.* **2019**;141(44):17763–70.
- Yu DS, Ma YC, Hu F, Lin CC, Li LL, Chen HY, Han XP, Peng SJ. Dual-sites coordination engineering of single atom catalysts for flexible metal–air batteries. *Adv Energy Mater.* **2021**;11:2101242.
- Zhang W, Fu Y, Liu W, Lim L, Wang X, Yu A. A general approach for fabricating 3D MFe₂O₄ (M=Mn, Ni, Cu, Co)/graphitic carbon nitride covalently functionalized nitrogen-doped graphene nanocomposites as advanced anodes for lithium-ion batteries. *Nano Energy.* **2019**;57:48–56.
- Chang H, Guo YF, Liu X, Wang PF, Xie Y, Yi TF. Dual MOF-derived Fe/N/P-tridoped carbon nanotube as high-performance

- oxygen reduction catalysts for zinc-air batteries. *Appl Catal B*. **2023**;327:122469.
28. Jia G, Zhang W, Fan G, Li Z, Fu D, Hao W, Yuan C, Zou Z. Three-dimensional hierarchical architectures derived from surface-mounted metal-organic framework membranes for enhanced electrocatalysis. *Angew Chem Int Ed*. **2017**;56(44):13781–5.
 29. Yang H, Chen Z, Kou S, Lu G, Chen D, Liu Z. Carbon-supported catalysts with atomically dispersed metal sites for oxygen electroreduction: present and future perspectives. *J Mater Chem A*. **2021**;9(29):15919–36.
 30. Niu W, Pakhira S, Marcus K, Li Z, Mendoza-Cortes JL, Yang Y. Apically dominant mechanism for improving catalytic activities of N-doped carbon nanotube arrays in rechargeable zinc–air battery. *Adv Energy Mater*. **2018**;8(20):1800480.
 31. Fu Y, Yu Z, Guo S, Li Y, Peng Q, Zhang L, Wu S, Han S. Catalytic effect of bamboo-like carbon nanotubes loaded with NiFe nanoparticles on hydrogen storage properties of MgH₂. *Chem Eng J*. **2023**;458: 141337.
 32. Zhang R, Zhang Y, Wei F. Horizontally aligned carbon nanotube arrays: growth mechanism, controlled synthesis, characterization, properties and applications. *Chem Soc Rev*. **2017**;46(12):3661–715.
 33. Xie L, Yu X, Wang S, Wei S, Hu Q, Chai X, Ren X, Yang H, He C. A multiscale strategy to construct cobalt nanoparticles confined within hierarchical carbon nanofibers for efficient CO₂ electroreduction. *Small*. **2022**;18(1): e2104958.
 34. Zhou T, Zhang N, Wu C, Xie Y. Surface/interface nanoengineering for rechargeable Zn–air batteries. *Energy Environ Sci*. **2020**;13(4):1132–53.
 35. Chen G, Lu R, Li C, Yu J, Li X, Ni L, Zhang Q, Zhu G, Liu S, Zhang J, et al. Hierarchically porous carbons with highly curved surfaces for hosting single metal FeN₄ sites as outstanding oxygen reduction catalysts. *Adv Mater*. **2023**;35(32): e2300907.
 36. Zhang S, Peng D, Xie H, Zheng Q, Zhang Y. Investigation on the formation mechanism of double-layer vertically aligned carbon nanotube arrays via single-step chemical vapour deposition. *Nano Lett*. **2017**;9(1):12.
 37. Chen S, Zhou X, Liao J, Yang S, Zhou X, Gao Q, Zhang S, Fang Y, Zhong X, Zhang S. FeNi intermetallic compound nanoparticles wrapped with N-doped graphitized carbon: a novel cocatalyst for boosting photocatalytic hydrogen evolution. *J Mater Chem A*. **2020**;8(6):3481–90.
 38. Charlier JC, Amara H, Lambin P. Catalytically assisted tip growth mechanism for single-wall carbon nanotubes. *ACS Nano*. **2007**;1(3):202–7.
 39. Duan X, Ren S, Pan N, Zhang M, Zheng H. MOF-derived Fe, Co@N–C bifunctional oxygen electrocatalysts for Zn–air batteries. *J Mater Chem A*. **2020**;8(18):9355–63.
 40. Qiao Y, Pan Y, Zhang J, Wang B, Wu T, Fan W, Cao Y, Mehmood R, Zhang F, Zhang F. Multiple carbon interface engineering to boost oxygen evolution of NiFe nanocomposite electrocatalyst. *Chin ese J Catal*. **2022**;43(9):2354–62.
 41. Tian X, Zhao X, Su YQ, et al. Engineering bunched Pt–Ni alloy nanocages for efficient oxygen reduction in practical fuel cells. *Science*. **2019**;366(6467):850–6.
 42. Jiao L, Zhu J, Zhang Y, Yang W, Zhou S, Li A, Xie C, Zheng X, Zhou W, Yu SH, et al. Non-bonding interaction of neighboring Fe and Ni single-atom pairs on MOF-derived N-doped carbon for enhanced CO₂ electroreduction. *J Am Chem Soc*. **2021**;143(46):19417–24.
 43. Deng C, Su Y, Li F, Shen W, Chen Z, Tang Q. Understanding activity origin for the oxygen reduction reaction on bi-atom catalysts by DFT studies and machine-learning. *J Mater Chem A*. **2020**;8(46):24563–71.
 44. Xu J, Lai S, Qi D, Hu M, Peng X, Liu Y, Liu W, Hu G, Xu H, Li F, et al. Atomic Fe–Zn dual-metal sites for high-efficiency pH-universal oxygen reduction catalysis. *Nano Res*. **2020**;14(5):1374–81.
 45. Huang HJ, Huang AM, Liu D, Han WT, Kuo CH, Chen HY, Li LL, Pan H, Peng SJ. Tailoring oxygen reduction reaction kinetics on perovskite oxides via oxygen vacancies for low-temperature and knittable zinc–air batteries. *Adv Mater*. **2023**;35:2303109.
 46. Lian Y, Yang W, Zhang C, Sun H, Deng Z, Xu W, Song L, Ouyang Z, Wang Z, Guo J, et al. Unpaired 3d electrons on atomically dispersed cobalt centres in coordination polymers regulate both oxygen reduction reaction ORR activity and selectivity for use in zinc–air batteries. *Angew Chem Int Ed*. **2020**;59(1):286–94.
 47. Song L, Fan H, Wang T, Xiang T, Zhang M, Hu C, Zhou W, He J. Facile synthesis of Co, N enriched carbon nanotube and active site identifications for bifunctional oxygen reduction and evolution catalysis. *Energy Storage Mater*. **2021**;43:365–74.
 48. Tian Y, Wu Z, Li M, Sun Q, Chen H, Yuan D, Zhang S. Atomic modulation and structure design of fen₄ modified hollow carbon fibers with encapsulated Ni nanoparticles for rechargeable Zn–air batteries. *Adv Funct Mater*. **2022**;32(52):2209273.
 49. Jiang M, Fu C, Cheng R, Zhang W, Liu T, Wang R, Zhang J, Sun B. Integrated and binder-free air cathodes of Co₃Fe₇ nanoalloy and Co_{5,47}N encapsulated in nitrogen-doped carbon foam with superior oxygen reduction activity in flexible aluminum–air batteries. *Adv Sci*. **2020**;7(18):2000747.
 50. Liu H, Li X, Peng C, Zhu L, Zhang Y, Cheng H, Cui J, Wu Q, Zhang Y, Chen Z, et al. Activating the lattice oxygen in (Bi_{0.5}Co_{0.5})₂O₃ by vacancy modulation for efficient electrochemical water oxidation. *J Mater Chem A*. **2020**;8(26):13150–9.
 51. Song JN, Qiu SY, Hu F, Ding YH, Han SL, Li LL, Chen HY, Han XP, Sun CH, Peng SJ. Sub-2 nm thiophosphate nanosheets with heteroatom doping for enhanced oxygen electrocatalysis. *Adv Funct Mater*. **2021**;31:2100618.
 52. Li Q, Chen W, Xiao H, Gong Y, Li Z, Zheng L, Zheng X, Yan W, Cheong WC, Shen R, et al. Fe isolated single atoms on S, N codoped carbon by copolymer pyrolysis strategy for highly efficient oxygen reduction reaction. *Adv Mater*. **2018**;30(25): e1800588.
 53. Ding LP, McLean B, Xu Z, Kong X, Hedman D, Qiu L, Page AJ, Ding F. Why carbon nanotubes grow. *J Am Chem Soc*. **2022**;144(12):5606–13.
 54. Werder T, Walthe JH, Jaffe RL, Halicioglu T, Noca F, Koumoutsakos P. Molecular dynamics simulation of contact angles of water droplets in carbon nanotubes. *Nano Lett*. **2001**;1(12):697–702.
 55. Wu L, Li J, Shi C, Li Y, Mi H, Deng L, Zhang Q, He C, Ren X. Rational design of the FeS₂/NiS₂ heterojunction interface structure to enhance the oxygen electrocatalytic performance for zinc–air batteries. *J Mater Chem A*. **2022**;10(31):16627–38.
 56. Zhong XW, Zheng ZY, Xu JH, Xiao X, Sun CB, Zhang MT, Ma JB, Xu BM, Yu K, Zhang X, Cheng HM, Zhou GM. Flexible zinc-air batteries with ampere-hour capacities and wide-temperature adaptabilities. *Adv Mater*. **2023**;35:2209980.
 57. Jiao ML, Dai LX, Ren HR, Zhang MT, Xiao X, Wang BR, Yang JL, Liu BL, Zhou GM, Cheng HM. A polarized gel electrolyte for wide-temperature flexible zinc–air batteries. *Angew Chem Int Ed*. **2023**;62: e202301114.

Publisher's Note Springer Nature remains neutral with regard to jurisdictional claims in published maps and institutional affiliations.

Springer Nature or its licensor (e.g. a society or other partner) holds exclusive rights to this article under a publishing agreement with the author(s) or other rightsholder(s); author self-archiving of the accepted manuscript version of this article is solely governed by the terms of such publishing agreement and applicable law.